

Loosely-packed dynamical structures with partially-melted surface being the key for thermophilic argonaute proteins achieving high DNA-cleavage activity

Lirong Zheng^{1,†}, Hui Lu^{2,†}, Bing Zan^{1,†}, Song Li^{1,†}, Hao Liu¹, Zhuo Liu¹, Juan Huang², Yongjia Liu³, Fan Jiang¹, Qian Liu^{2,*}, Yan Feng² and Liang Hong^{1,*}

¹School of Physics and Astronomy, Institute of Natural Sciences, School of Medicine, Shanghai National Center for Applied Mathematics (SJTU center), Zhangjiang Institute for Advanced Study, Shanghai Jiao Tong University, Shanghai 200240, China, ²State Key laboratory for Microbial Metabolism, School of Life Sciences and Biotechnology, Shanghai Jiao Tong University, Shanghai 200240, China and ³Instrumental Analysis Center, Shanghai Jiao Tong University, Shanghai 200240, China

Received January 06, 2022; Revised May 19, 2022; Editorial Decision June 12, 2022; Accepted June 17, 2022

ABSTRACT

Prokaryotic Argonaute proteins (pAgos) widely participate in hosts to defend against the invasion of nucleic acids. Compared with the CRISPR-Cas system, which requires a specific motif on the target and can only use RNA as guide, pAgos exhibit precise endonuclease activity on any arbitrary target sequence and can use both RNA and DNA as guide, thus rendering great potential for genome editing applications. Hitherto, most in-depth studies on the structure-function relationship of pAgos were conducted on thermophilic ones, functioning at ~60 to 100°C, whose structures were, however, determined experimentally at much lower temperatures (20–33°C). It remains unclear whether these low-temperature structures can represent the true conformations of the thermophilic pAgos under their physiological conditions. The present work studied three pAgos, *PfAgo*, *TtAgo* and *CbAgo*, whose physiological temperatures differ significantly (95, 75 and 37°C). By conducting thorough experimental and simulation studies, we found that thermophilic pAgos (*PfAgo* and *TtAgo*) adopt a loosely-packed structure with a partially-melted surface at the physiological temperatures, largely different from the compact crystalline structures determined at moderate temperatures. In contrast, the mesophilic pAgo (*CbAgo*) assumes a compact crystalline structure at

its optimal function temperature. Such a partially-disrupted structure endows thermophilic pAgos with great flexibility both globally and locally at the catalytic sites, which is crucial for them to achieve high DNA-cleavage activity. To further prove this, we incubated thermophilic pAgos with urea to purposely disrupt their structures, and the resulting cleavage activity was significantly enhanced below the physiological temperature, even at human body temperature. Further testing of many thermophilic Agos present in various thermophilic prokaryotes demonstrated that their structures are generally disrupted under physiological conditions. Therefore, our findings suggest that the highly dynamical structure with a partially-melted surface, distinct from the low-temperature crystalline structure, could be a general strategy assumed by thermophilic pAgos to achieve the high DNA-cleavage activity.

INTRODUCTION

Programmable endonucleases have revolutionized genome-editing technologies, such as molecular diagnostics and genetic modification, which are critical for life science, biosecurity, medical treatment, and environmental monitoring (1–3). In recent years, the clustered regularly interspaced short palindromic repeats (CRISPR)-Cas system has attracted great attention, which enabled target nucleic acids to be manipulated at a specific spot, thus leading to changes in physical traits and achieving medical diagnostics (4–8).

*To whom correspondence should be addressed. Tel: +86 021 54742996; Fax: +86 021 54742996; Email: hongli3liang@sjtu.edu.cn
Correspondence may also be addressed to Qian Liu. Email: liuqian1018@sjtu.edu.cn

†The authors wish it to be known that, in their opinion, the first four authors should be regarded as Joint First Authors.

Reminiscent of the CRISPR-Cas system, Argonaute proteins (*Ago*s) are nucleic acid-guided endonucleases, which have been proposed to be suitable candidates for a range of biotechnological applications (9–12). Whereas Cas nucleases require the presence of a protospacer-adjacent motif (PAM) or protospacer flanking site (PFS) (13), *Ago*s are independent of such motifs. Furthermore, *Ago*s can utilize DNA as guides that are much easier to produce and more stable during application than the RNA guides used by CRISPR-Cas. All the above advantages give *Ago*s potential for easy-to-implement and high-throughput screenings in gene editing and medical diagnostics (10–12,14,15).

*Ago*s are widely distributed in all three domains of life (16). Eukaryotic Argonaute proteins (*eAgo*s) are key players in RNA interference, while prokaryotic Argonaute proteins (*pAgo*s) participate in host defense by DNA interference (16,17). Most *eAgo*s and *pAgo*s share similar two-lobed structures, with the C-terminal lobe consisting of the middle (MID) and PIWI domains and the N-terminal lobe containing the N-terminal and PIWI-Argonaute-Zwille (PAZ) domains (14,18). Structural studies have identified that *pAgo*s bind guide strands, of which the 5'-end and 3'-end are anchored in the barrel-like pocket of the MID domain and the PAZ domain, respectively, serving as a template for binding complementary target strands (19,20). When anchoring to the protein, the conformation of the guide strand is organized to achieve high binding affinity to the target strand (20–22). The binding between the guide and target initiates in the seed region and then propagates along the guide. After this, the 3'-end of the guide is released from the PAZ domain, accompanied by a large conformational change in the protein (18,19,23), and then the PIWI domain cleaves the phosphodiester bond of the target between the 10th and 11th bases counted from the 5'-end of the guide (19,22,24).

Although the cleavage function and overall fold among *pAgo*s are similar, their physiological functional temperatures, T_{phy} , are vastly different (16). For instance, *Pyrococcus furiosus Ago* (*PfAgo*) and *Thermus thermophilus Ago* (*TtAgo*) are most active in the temperature range from 87–99.9°C (24) and 75–86°C (10), respectively, while *Clostridium butyricum Ago* (*CbAgo*) (25) and *Kurthia massiliensis Ago* (*KmAgo*) (26) display the highest cleavage activity at human body temperature (37°C). The intriguing question then arises as to what structural factors control the thermostability among different *pAgo*s. To date, the structure-function relationship of *pAgo*s has typically been normally derived from their crystal structures determined at moderate temperatures (20–33°C) (19,25,27). It remains unclear whether these low-temperature crystal structures represent the true functional conformations of thermophilic *pAgo*s at their physiological temperature, T_{phy} , which is much greater than the temperature at which the crystal structure is determined.

In the present study, by combining synchrotron small-angle X-ray scattering (SAXS), circular dichroism spectroscopy (CD spectroscopy), nano differential scanning calorimetry (nanoDSC), differential scanning fluorimetry (DSF), molecular dynamics (MD) simulation and biochemical assays, we studied the structure, dynamics, and endonuclease activity of thermophilic *pAgo*s (*PfAgo* and *TtAgo*)

and their mesophilic counterpart *CbAgo* as well as the temperature dependences. We found that, compared to *CbAgo*, the two thermophilic *pAgo*s possess stronger intramolecular interactions (salt bridges, hydrogen bonds and hydrophobic interactions) both globally over the entire protein and locally at the catalytic residues. Not only do these stronger intramolecular interactions impart thermostability to thermophilic *pAgo*s but they could also be the key to limiting the endonuclease activity of these proteins at moderate temperatures. Furthermore, we demonstrated that, at physiological temperatures, thermophilic *pAgo*s are loosely packed with a partially-melted surface, different from the crystalline structure. In contrast, mesophilic *CbAgo* assumes a compact conformation analogous to its crystalline structure at its T_{phy} . We showed that the partially-disrupted structure renders the two thermophilic *pAgo*s (*PfAgo* and *TtAgo*) a significant degree of flexibility by reducing the strong intramolecular interactions, which could be crucial for them to achieve high endonuclease activity at physiological temperatures. To further prove this, we partially unfolded the two thermophilic *pAgo*s by incubating them with denature agents and found that this indeed greatly enhanced their DNA-cleavage activity. Further results on other thermophilic *pAgo*s suggest that the partially-disrupted structure could be a general feature for them to function under physiological conditions.

MATERIALS AND METHODS

Protein expression and purification

A codon-optimized version of the *PfAgo*, *TtAgo* and *CbAgo* gene was synthesized by Sangon Biotech (Shanghai, China), and was cloned into the pET28a plasmid to construct pEX-*PfAgo* (*TtAgo* and *CbAgo*) with an N terminal His-tag. The expression plasmid was transformed into *Escherichia coli* BL21(DE3) cells. A 10 ml seed culture was grown at 37°C in LB medium with 50 µg/ml kanamycin and was subsequently transferred to 1 L of LB in a shaker flask containing 50 µg/ml kanamycin. The cultures were incubated at 37°C until the OD₆₀₀ reached 0.8–1.0, and protein expression was then induced by the addition of isopropyl-D-thiogalactopyranoside (IPTG) to a final concentration of 0.5 mM, followed by incubation for 20–24 h at 18°C. Cells were harvested by centrifugation for 30 min at 6000 rpm, and the cell pellets were collected for later purification. The cell pellets were resuspended in lysis buffer (20 mM Tris-HCl, 1 M NaCl, pH 8.0) and then disrupted using a High-Pressure Homogenizer at 700–800 bar for 5 min (Gefran, Italy). The lysates were centrifuged for 30 min at 12 000 rpm at 4°C, after which the supernatants were subjected to Ni-NTA affinity purification with elution buffer (20 mM Tris-HCl, 1 M NaCl, 200 mM imidazole, pH 8.0). Further gel filtration purification using a Superdex 200 (GE Tech, USA) was carried out with elution buffer (20 mM Tris-HCl, 1 M NaCl, pH 8.0). The fractions resulting from gel filtration were analyzed by SDS-PAGE, and fractions containing the protein were flash frozen at –80°C in storage buffer I (PBS, pH 8.0) and buffer II (20 mM Tris-HCl, pH 8.0, 250 mM NaCl). Buffer I was used for CD spectra and buffer II was used for other assays. The SDS-PAGE analysis of *PfAgo*, *TtAgo* and *CbAgo* are shown in Supplementary Figure S34.

Circular dichroism (CD) spectroscopy

The CD measurements on the evolution of the secondary structure of ligand-free pAgos were performed in a Jasco J-1500 spectropolarimeter with a 1 mm pathlength cell. The signals in the far-UV CD region (222 nm) were monitored as a function of temperature to determine the thermal unfolding of pAgos. The concentrations of pAgos were 0.1 mg/ml in 1× PBS buffer (pH 8.0) for the various measurements. The pAgos were heated in the range of 15°C to 100°C with a 1°C/min heating rate and equilibrated for 3 min at each temperature, and the CD data were collected at 0.5°C intervals. For CD spectra, we used PBS buffer as solvent instead of Tris–HCl buffer because the Tris–HCl buffer has a strong CD background, which will significantly affect analysis of the CD signal of proteins (see Supplementary Figure S33).

Chemical denaturation study of proteins

To determine the stability curves at 298 K, samples of ligand-free *PfAgo*, *TtAgo* and *CbAgo* in 1× PBS buffer (pH 8.0) were incubated with urea of different concentrations ranging from 0–14 M for 24 h. Then, the far-UV CD spectra were used to analyze the structure of the resulting proteins at 298 K.

Differential scanning fluorimetry (DSF)

Each pAgo sample containing 2 μM of protein in a buffer containing 15 mM Tris–HCl (pH 8.0) and 250 mM NaCl was prepared in triplicate and added to PCR tubes. SYPRO Orange dye available as 5000× stock (Sigma-Aldrich) was added just before the measurement of the ligand-free pAgos in an appropriate amount to achieve a final concentration of the dye of 5×. The thermal denaturation of the pAgos was monitored by exciting the SYPRO Orange dye at 470 nm and monitoring its fluorescence emission at 570 nm using Q-PCR (Analytikjena, Germany). The baseline correction is used by the Opticon Monitor software available on the PCR instrument.

Nano differential scanning calorimetry (nanoDSC)

nanoDSC measurements were performed by using Nano DSC instruments (TA, USA). The concentration of pAgos was 0.5 mg/ml in a buffer containing 15 mM Tris–HCl (pH 8.0) and 250 mM NaCl. All the experiments were carried out at temperatures ranging from 10 to 110°C with a heating rate of 1°C/min and under a pressure of 3 atm. The melting curves of pAgos were subtracted from the buffer scans.

Small angle X-ray scattering (SAXS)

SAXS measurement was employed to monitor the structural evolution of pAgos during heating conditions. In-situ synchrotron SAXS measurements were conducted at BL19U2 beamline in Shanghai Synchrotron Radiation Facility (SSRF). The X-ray wavelength was 0.103 nm. Protein samples were dissolved in a buffer containing 20 mM Tris–HCl (pH 8.0), 250 mM NaCl and 2 mM DTT. The concentration of samples is ~0.3 mg/ml. Protein solutions were

loaded into the silica cell and then gently refreshed with a syringe pump to prevent X-ray damage. The measurements were carried out at different temperatures ranging from 10–100°C and samples were reloaded into the cell at each temperature. In order to calculate the absolute intensity of protein, the empty cell and buffer were also measured at corresponding temperatures. Two-dimensional (2D) diffraction patterns were collected by the Pilatus 2 M detector with a resolution of 1043 × 981 pixels of 172 μm × 172 μm. Twenty sequential 2D images were collected with 0.5 s exposure time per frame. The 2D scattering patterns were then integrated into one-dimensional (1D) intensity curves by using Fit2D software from European Synchrotron Radiation Facility (ESRF). Frames with no radiation damage were used for further processing. *ab initio* reconstruction of protein structure by a chain-like ensemble of dummy residues is generated by GASBOR (28). P1 (no symmetry) and monodisperse data mode were used in generating GASBOR model. At least 10 iterations of GASBOR programs were independently performed to validate the models. A representative of the most typical model obtained was used in the figures. The SAXS data was compared to atomic model by using CRY SOL software (29). The one-dimensional data is processed by using *Scatter* and ATSAS software. The details of SAXS data collection and analysis are summarized in Supplementary Table S5.

Single-strand DNA cleavage assay

For standard activity assays, cleavage experiments were performed in a 1:10:5 molar ratio (pAgo:guide:target). First, 800 nM pAgo was mixed with synthetic 8 μM ssDNA guide and with a certain amount of urea, which is 0.64 M for *TtAgo*, 1.28 M for *PfAgo* and 2 M for *CbAgo* in the reaction buffer (15 mM Tris–HCl (pH 8.0), 250 mM NaCl, 0.5 mM MnCl₂ for *PfAgo*, MgCl₂ for *TtAgo* and *CbAgo*). The solution was then preincubated at 25°C for 24 h. After preincubation, 4 μM ssDNA target, which was labeled with the fluorescent group 6-FAM at the 5'-end and the quencher BHQ1 at the 3'-end, was added to the mixture. The cleavage experiments were performed at different temperatures to obtain the temperature-dependent enzymatic activity. All experiments were performed in triplicate, and the fluorescence signals were traced by the quantitative real-time PCR QuantStudio 5 (Thermo Fisher Scientific, USA) with λ_{ex} = 495 nm and λ_{em} = 520 nm. The results were analyzed by QuantStudio™ Design & Analysis Software v1.5.1 and GraphPad Prism 8.0. For the kinetic measurements, the parameters *k*_{cat} and *K*_M were determined by fitting the Michaelis–Menten equation to the velocity of each reaction as a function of the concentration of ssDNA target. Here, eight different concentrations of the ssDNA target, ranging from 0.2 to 8 μM, were used. The results were analyzed by QuantStudio™ Design & Analysis Software v1.5.1 and GraphPad Prism 8.0. The cleavage rate of pAgos was determined by the maximum slope of the fluorescence intensity-time curves (see in Supplementary Figures S17 and S18). The product concentration *c*_p versus time was calculated using the following equation:

$$c_p(t) = \frac{F(t) - F_0}{F_m - F_0} \times c_s$$

where c_s is the initial concentration of ssDNA substrate, $F(t)$ is the fluorescence value measured at a certain time, F_0 is the initial fluorescence value of ssDNA substrate, and F_m is the fluorescence value measured at the condition where the substrates react with excess *PfAgo* at 95°C for 30 min.

The ssDNA cleavage assay of *PfAgo* at 37°C was carried out in the reaction buffer. To obtain the partially unfolded state in *PfAgo* at 37°C, *PfAgo* and 6 M urea were mixed and then incubated at 25°C for 24 h to reach the equilibrium state. For ssDNA cleavage, 800 nM *PfAgo*, 8 μM ssDNA guide and 4 μM ssDNA target were mixed in the reaction buffer and then incubated for 15 min at 37°C in a thermocycler. The reaction time was set as 5, 7, 10, 18, 21 and 24 h at 37°C. Following the different reaction times, the samples were cooled by slowly lowering the temperature at a rate of 0.1°C/s until it reached 10°C. The addition of loading buffer (95% formamide, 0.5 mmol/l EDTA, 0.025% bromophenol blue, 0.025% xylene cyanol) at a 1:1 ratio (v/v) stopped the reactions. The samples were then separated in 16% denaturing polyacrylamide gels and analyzed by staining with GelRed (Biotium, USA). The nucleic acids were visualized using a Tanon 3500BR (Shanghai, China), and the data were analyzed using Quantity One (Bio-Rad, USA).

The ssDNA cleavage assay of *CbAgo* was carried out in the reaction buffer. *CbAgo* and 2 M (0.64 M) urea were mixed and then incubated at 25°C for 24 h to reach the equilibrium state. For the ssDNA cleavage experiment, 800 nM *CbAgo*, 8 μM ssDNA guide, and 4 μM ssDNA target were mixed in the reaction buffer. The reaction temperature was set as 1 h at 20, 30, 34, 37, 42 and 46°C. Following the different reaction temperatures, the samples were cooled by slowly lowering the temperature at a rate of 0.1°C/s until it reached 10°C. The addition of loading buffer (95% formamide, 0.5 mmol/l EDTA, 0.025% bromophenol blue, 0.025% xylene cyanol FF) at a 1:1 ratio (v/v) stopped the reactions. The samples were then separated in 16% denaturing polyacrylamide gels and analyzed by staining with GelRed (Biotium, USA). The nucleic acids were visualized using a Tanon 3500BR (Shanghai, China), and the data were analyzed using Quantity One (Bio-Rad, USA).

Molecular dynamics (MD) simulations

Simulation of the proteins in aqueous solution. The initial structures of *PfAgo*, *TtAgo* and *CbAgo* for simulations were taken from PDB crystal structures 1Z26 (27), 4N47 (19) and 6QZK (25), respectively. It should be noted that the guide DNA, target DNA and metal ions (Mn^{2+} and Mg^{2+}) were removed from proteins before performing MD simulation. Two protein monomers were filled in a cubic box (see Supplementary Figure S2). A large amount of water molecules was filled into the box to mimic the experimental concentration. Then, 16 chlorine counter ions were added to keep the system neutral in charge. The CHARMM36m force field (30) was used for *pAgos*, and the CHARMM modified TIP3P model was chosen for water. The simulations were carried out at 283, 298 and 310 K. After the 4000-steps energy-minimization procedure, the systems were heated and equilibrated for 100 ps in the NVT ensemble and 500 ps in the NPT ensemble. The 100-ns production simulations were carried out at 1 atm with the proper periodic bound-

ary condition, and the integration step was set to 2 fs. Supplementary Figure S3 shows the 100 ns profile of potential energy as a function of MD trajectory time for *PfAgo*, *TtAgo* and *CbAgo*. It was clear that the equilibration procedure was sufficient for energy minimalization of protein structures, i.e. the proteins adopted the stable conformations with minimum energy after equilibration. The covalent bonds with hydrogen atoms were constrained by the LINCS algorithm (31). Lennard–Jones interactions were truncated at 12 Å with a force switching function from 10 to 12 Å. The electrostatic interactions were calculated using the particle mesh Ewald method (32) with a cutoff of 12 Å on an ~1 Å grid with a fourth-order spline. The temperature and pressure of the system are controlled by the velocity rescaling thermostat (33) and the Parrinello–Rahman algorithm (34), respectively. All MD simulations were performed using GROMACS 2020.4 software packages. Representative simulation snapshots of the systems are given in Supplementary Figure S2.

The classification of surface amino acid residues and internal amino acid residues is based on the solvent-accessible surface area (SASA). The number of hydrogen bonds and salt bridges are estimated from GROMACS 2020.4 software packages. The relative content of hydrophobic residues in the core of the protein is defined as the ratio of the number of hydrophobic residues to that of the overall internal residues.

Simulation of the proteins in urea solution. To identify the effect of urea molecules on the structure and dynamics of *PfAgo*, we conducted a simulation of *PfAgo* solution in the presence of urea. The initial structure of *PfAgo* was taken from PDB crystal structure 1Z26, and one monomer protein was filled in a cubic box. The water and 6 M urea molecules were randomly inserted into the box to mimic the experimental concentration. Then, 8 chlorine counter ions were added to neutralize the system. The CHARMM36m force field (30) (version March, 2019) and the CHARMM-modified TIP3P model were used for protein and solvent, respectively. The CHARMM-compatible stream file of urea molecules was generated by the online CGenFF server (35,36). Then the GROMACS conversion program ‘cgenff_charmm2gmx_py3.py’ and CHARMM36m force field were used to generate the urea parameters for GROMACS (30). The simulations were carried out at 310 K. After the 4000-steps energy-minimization procedure, the systems were heated and equilibrated for 100 ps in the NVT ensemble and 500 ps in the NPT ensemble. The temperature and pressure of the system are controlled by the velocity rescaling thermostat (33) and the Berendsen barostat (34), respectively. The 100-ns production simulations were carried out with the proper periodic boundary condition, and the integration step was set to 2 fs (a snapshot of the MD simulation of (Supplementary Figure S26a) *PfAgo* with 6 M urea and (Supplementary Figure S26b) *PfAgo* in solution). Supplementary Figure S27 shows the 100 ns profile of potential energy as a function of MD trajectory time for *PfAgo* with and without 6 M urea. It was clear that the equilibration procedure was sufficient for energy minimalization of protein structures, i.e. the proteins adopted the stable conformations with minimum energy after equilibration. It

should be noted that 11 500 urea molecules were added to the whole simulation system to mimic the experimental conditions so that the NVT ensemble was used in the production simulation to avoid system collapse. The covalent bonds with hydrogen atoms were constrained by the LINCS algorithm (31). Lennard–Jones interactions were truncated at 12 Å with a force switching function from 10 to 12 Å. The electrostatic interactions were calculated using the particle mesh Ewald method (32) with a cutoff of 12 Å on an approximately 1 Å grid with a fourth-order spline. The simulation was performed using GROMACS 2020.4 software packages.

To exclude the effect of simulation time on the number of hydrogen bonds and salt bridges in proteins, we extended the simulation time to 500 ns on *PfAgo* with and without 6 M urea. We calculated the number of hydrogen bonds and salt bridges globally over the entire protein and locally at catalytic sites. As shown in Supplementary Figures S29 and S30, the extended simulation times do not induce further reduction in hydrogen bonds and salt bridges.

RESULTS AND DISCUSSION

Comparison of thermostability between different pAgos and revealing the underlying structural mechanism

The thermal stability of the three pAgos was examined by nanoDSC, and the obtained thermal-melting curves are presented in Figure 1A, showing that the melting temperatures (T_m) of *CbAgo*, *TtAgo* and *PfAgo* are 46, 75 and 100°C, respectively. Moreover, the unfolding free-energy barrier, ΔG_u , can be estimated from the chemical-induced unfolding curves determined by far-UV spectra and ranks as *PfAgo* > *TtAgo* > *CbAgo* (see Figure 1B and Supplementary Figure S1). Both Figure 1A and B demonstrates that the two thermophilic pAgos have much greater thermostability than the mesophilic *CbAgo*.

We then compared the crystalline structures of *PfAgo*, *TtAgo* and *CbAgo* reported in Refs. (19,25,27). As shown in Figure 1C and D, all the three pAgos assume a two-lobed molecular architecture, typical for the family of long pAgos (14). The superposition of the crystalline structures of the three proteins is shown in Figure 1D, revealing that they share similar tertiary folding. However, a detailed analysis of the secondary structures (see Supplementary Table S1) shows that the two thermophilic pAgos have slightly fewer loops and turns than *CbAgo*.

To further explore the structural factors responsible for the thermostability, we conducted MD simulation on these three pAgos in the apo state without guide, target DNA or divalent cations at 298 K and analyzed the important intramolecular interactions (a snapshot of the MD simulation of pAgos is shown in Supplementary Figure S2, and the potential energy as a function of MD trajectory time of proteins is shown in Supplementary Figure S3). As shown in Figure 1E, the two thermophilic pAgos possess a much greater amount of hydrogen bonds and salt bridges than *CbAgo*. In addition, the thermophilic pAgos have stronger hydrophobic interactions inside the protein core than *CbAgo* (see Supplementary Table S2). These additional inter-residue interactions and a smaller number of

flexible loops and turns in the thermophilic pAgos will render them greater thermostability as compared to *CbAgo*. Moreover, these structural factors will inevitably suppress the structural flexibility of thermophilic pAgos, and this was confirmed by analysis of B-factors derived from crystal structures and MD (Supplementary Figures S4 and S5), showing that the two thermophilic pAgos were globally stiffer than *CbAgo*.

Furthermore, we also analyzed the intramolecular interaction around the catalytic region. The PIWI domain of *PfAgo*, *TtAgo* and *CbAgo* adopts an RNase H-like fold with the highly conserved catalytic tetrad of Asp-Glu-Asp-X (DEDX, X = Asp, Asn or His) (19,24,25,37) (see the lower panel in Figure 1D). We found that the numbers of hydrogen bonds and salt bridges formed between the catalytic tetrad and the surrounding amino acid residues are significantly larger in *PfAgo* and *TtAgo* than in *CbAgo* (see Figure 1F). One can thus deduce that the stronger inter-residue interactions around the catalytic site in thermophilic pAgos will provide thermostability to the catalytic region and inevitably rigidify the local structure. The latter is confirmed by Supplementary Figures S6 and S7, where the B-factor of the catalytic tetrad is indeed smaller in *PfAgo* and *TtAgo* than in *CbAgo*.

It has been reported that conformational rearrangements are essential to the cleavage process of pAgos, such as guide binding (20,38), releasing the 3'-end guide from the PAZ domain after duplex propagation (19,22,39), and alignment of catalytic residues in the PIWI domain for cleavage and release of the cleaved target (19,22). As discussed above, the structural flexibility of the two thermophilic pAgos is strongly suppressed both locally at the catalytic site (Supplementary Figures S6 and S7) and globally over the entire protein (Supplementary Figures S4 and S5) due to strong intramolecular interactions (Figure 1E and F) and fewer flexible loops and turns (Supplementary Table S1). Such structural rigidity might limit their endonuclease functionality at moderate temperatures. For example, at 37°C, *PfAgo* exhibits only a small fraction (~5%) of cleavage activity as achieved at 95°C (24).

The microscopic origin of the stability of thermophilic proteins is also discussed in other simulation work (40,41). Ref. (40) and Ref. (41) demonstrated that the electrostatic interactions between charged residues are more favored in thermophilic proteins to render their stability as compared to their mesophilic counterparts. F. Sterpone *et al.* (41) pointed out that the stability of thermophilic proteins can be attributed to many factors, including stronger inter-residue interactions inside the protein, i.e. enthalpy-driven mechanisms, entropic reservoir formed by fluctuations, i.e. the flexibility of biomacromolecules, and the role of solvents. In the present study, we found that the structural flexibility of the two thermophilic pAgos is strongly suppressed both locally at the catalytic site and globally over the entire protein because the thermophilic pAgos possess a larger number of strong inter-residue interactions, including hydrogen bonds, salt bridges and hydrophobic interactions, as well as fewer flexible loops and turns than mesophilic *CbAgo*. This stiff structure in thermophilic pAgos could reduce the functional flexibility and thus may lead to low cleavage activity at moderate temperature. The previous

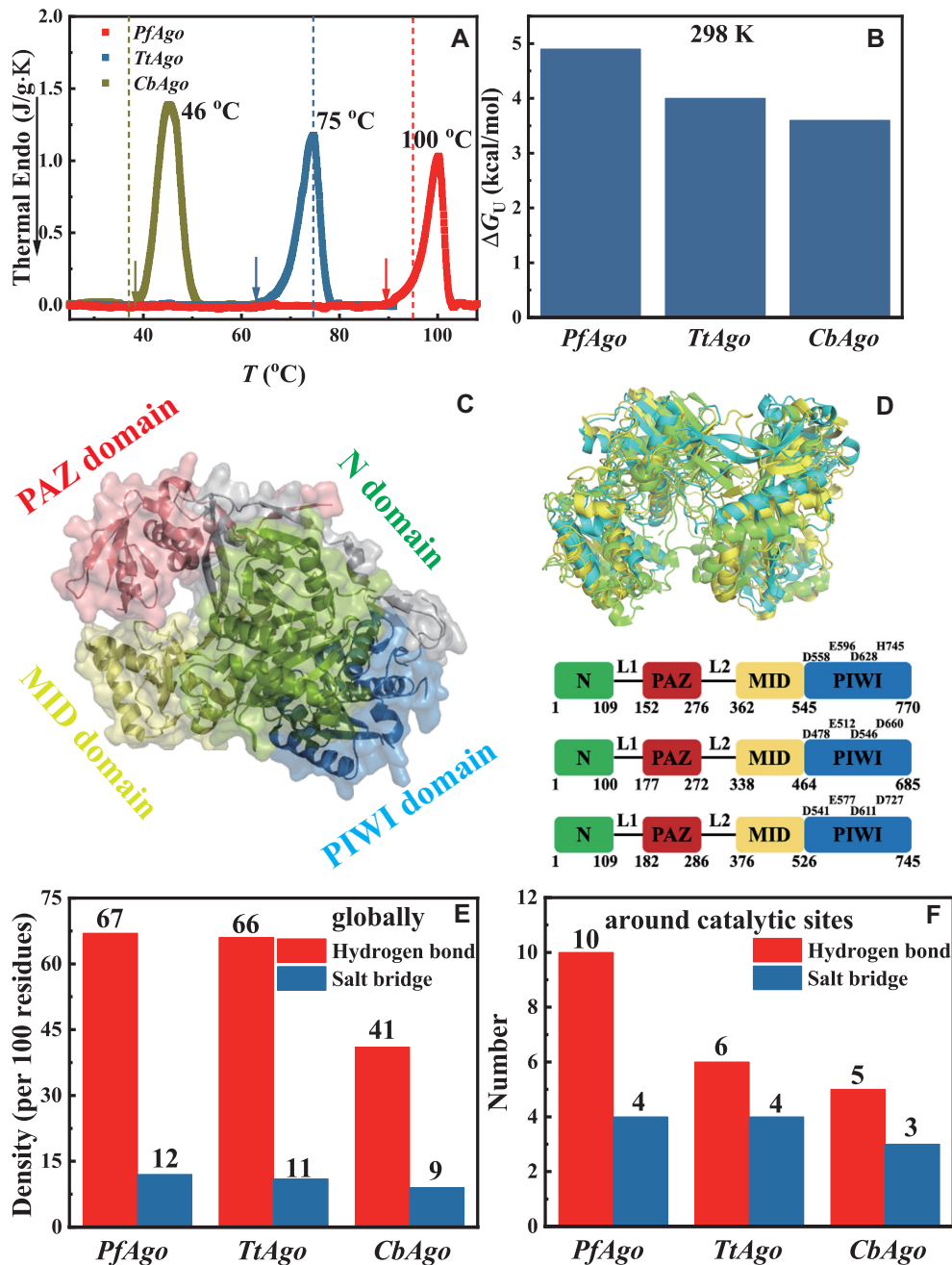


Figure 1. Structural and dynamical analysis of *PfAgo*, *TtAgo* and *CbAgo*. (A) Thermal denaturation curves of *pAgo*s determined by nanoDSC, where the melting temperature (T_m) values are presented. The solid arrows and dashed lines represent the onset of unfolding temperature (T_{on}) and the physiological temperature (T_{phy}), respectively. (B) Free-energy difference between a well-folded protein and a fully-unfolded state at 298 K derived from the urea-induced unfolding curve measured by far-UV CD spectra. The detailed procedure is presented in Materials and Methods and ref. (55). (C) Representation of the domain architectures of *pAgo*s. The PAZ domain, MID domain, N domain, and PIWI domain are colored in red, yellow, green, and blue, respectively. (D) Upper panel: Superposition of the crystalline structures of *PfAgo* (green, PDB ID: 1z26), *TtAgo* (blue, PDB ID: 4n47) and *CbAgo* (yellow, PDB ID: 6qzk). Lower panel: Schematic diagram of the domain organization of *PfAgo*, *TtAgo* and *CbAgo*. (E) The density of hydrogen bonds and salt bridges in *PfAgo*, *TtAgo* and *CbAgo* over the entire biomolecule obtained from MD simulation. (F) The number of hydrogen bonds and salt bridges formed between catalytic sites and surrounding amino acid residues in *PfAgo*, *TtAgo* and *CbAgo* obtained from MD simulation.

works alongside the present study all point to an important rule that the strong inter-residue interaction, particularly the electrostatic interactions, inside the protein play an important role in stabilizing the protein and reducing the structural flexibility.

Thermophilic pAgo takes a loosely-packed and partially-disrupted dynamical structure under physiological conditions

Characterization by CD, DSF and nanoDSC. Although the detailed structures of pAgo with or without substrates have been revealed by X-ray crystallography at moderate temperatures, the in situ characterization of the structure at physiological temperatures has not been conducted. Here, far-UV CD spectra were applied to characterize the temperature dependence of the secondary structures of the three pAgo without guide DNA, target DNA and divalent cations (Mg^{2+} or Mn^{2+}). Figure 2A–C displays the far-UV CD spectra of the three pAgo measured at different temperatures. The spectra of *CbAgo* have an explicit isochromatic point, where the dichroic angle, θ , at a given absorbance wavelength collapses to a single constant value at different temperatures during the unfolding process (highlighted by the dashed red circle in Figure 2A). However, such an isochromatic point is absent in both *PfAgo* and *TtAgo* (Figure 2B and C). The presence of a well-defined isochromatic point is crucial evidence for the two-state scenario that the ensemble consists of two components during the thermal unfolding process: the well-folded protein and the fully-unfolded one, and the relative population of the fully-unfolded protein is increased upon heating (42–44). In contrast, the absence of the isochromatic point in thermophilic pAgo implies that stable intermediate states exist between the well-folded structure and fully-unfolded structure during thermal unfolding (42–44).

Moreover, Figure 2D displays the thermal unfolding curves of the three pAgo measured by far-UV CD spectra by monitoring the intensity of the 222 nm wavelength characterizing the content of the alpha helix. We found that T_{phy} of *CbAgo* (marked by the dashed line) was lower than the onset temperature of thermal unfolding, T_{on} (marked by the solid arrow). This result suggests that *CbAgo* assumes a non-disrupted well-folded structure under physiological conditions. In sharp contrast, the T_{phy} values of the two thermophilic pAgo are significantly higher than their T_{on} values, which is also supported by the nanoDSC results (see Figure 1A). Moreover, we also conducted DSF measurements to monitor the change in the tertiary structure of the three pAgo over the thermal unfolding process. Again, as shown in Figure 2e, the DSF measurement confirms the findings of far-UV CD spectra and nanoDSC. The observation of T_{phy} being higher than T_{on} (Figures 1A, 2D and E) and the absence of an isochromatic point (Figure 2B and C) in the two thermophilic pAgo indicate that they assume stable intermediate structures at their physiological condition where some of the secondary and tertiary structures present at moderate temperatures are disrupted. This observation is drastically different from that of *CbAgo*, which takes well-folded conformations when functioning. We further analyzed other thermophilic pAgo using DSF, including those in *Ferroglobus placidus* (*FpAgo*), *Thermococcus*

onmurineus (*ToAgo*), *Methanocaldococcus fervens* (*MfAgo*), and *Marinitoga Piezophile* (*MpAgo*). As shown in Supplementary Figure S8, for all thermophilic pAgo studied, T_{phy} was significantly higher than T_{on} . Hence, one can deduce that thermophilic pAgo might generally assume partially-disrupted structures at under physiological conditions.

The above analysis in Figures 1 and 2 was conducted on the protein without ligands. Further far-UV CD measurement was applied to monitor the secondary structure of pAgo in complex with ssDNA guide, complementary ssDNA target (the nucleotide sequence of guide and target ssDNA are presented in Supplementary Figure S9) and divalent cations (Mg^{2+} or Mn^{2+}) at both $10^{\circ}C$ and T_{phy} . At T_{phy} , the secondary structure of the *CbAgo* complex with guide DNA, target DNA and bound Mg^{2+} bound resembles that measured at $10^{\circ}C$ (Supplementary Figure S10a). In sharp contrast, the secondary structure of the two thermophilic pAgo complexes is partially melted at T_{phy} as compared to that at $10^{\circ}C$ (Supplementary Figure S10b and c). Therefore, the partially-disrupted structures in *PfAgo* and *TtAgo* are intrinsic in nature at T_{phy} , independent of whether the protein forms a complex with the guide, target and divalent cations.

Characterization by SAXS. To gain further detailed information on the dependence of the microscopic structure and dynamics of the proteins as a function of temperature, we conducted small-angle X-ray scattering (SAXS) on *PfAgo*, *TtAgo* and *CbAgo* in solution at different temperatures in Shanghai Synchrotron Radiation Facility (SSRF). SAXS has been widely used to characterize the overall shape, packing and flexibility of biomacromolecules (45–47). As seen in Supplementary Figure S11, the scattering profiles of all three pAgo collected at $10^{\circ}C$ agree with those calculated from the corresponding crystal structures using CRY SOL software (29), revealing that all pAgo in solution at $10^{\circ}C$ adopt structures mimicking the crystalline form.

Figure 3A–C displays the dimensionless Kratky plot for *PfAgo*, *TtAgo* and *CbAgo* at various temperatures (the original curves are presented in Supplementary Figure S12). Dimensionless Kratky plots are often used to qualitatively identify disordered states and distinguish them from the compact globular structure (47–51). The compact globular proteins confer a bell-shaped dimensionless Kratky plot with a well-defined maximum (e.g. see the dimensionless Kratky plots of lysozyme in Figure 3A–C) (48–50,52). Conversely, the dimensionless Kratky plot of an ideal random Gaussian chain or fully unfolded protein normally increases monotonically with q without showing any bell-shaped peak in the low q region and does not plateau at high q (e.g. see the dimensionless Kratky plots of intrinsically disordered protein (IDP) in Figure 3A–C) (48–50,52). We compared the dimensionless Kratky plot of each of the three pAgo at T_{phy} with respect to the corresponding plot measured at $10^{\circ}C$. As shown in Figure 3A, the dimensionless Kratky plot of *CbAgo* at T_{phy} is the same as that collected at $10^{\circ}C$, indicating that the mesophilic pAgo adopts the crystalline structure under its physiological condition. For *PfAgo* and *TtAgo*, when comparing to the results measured at $10^{\circ}C$, the dimensionless Kratky plots at T_{phy} show an explicit upthrow of the plateau at high qR_g

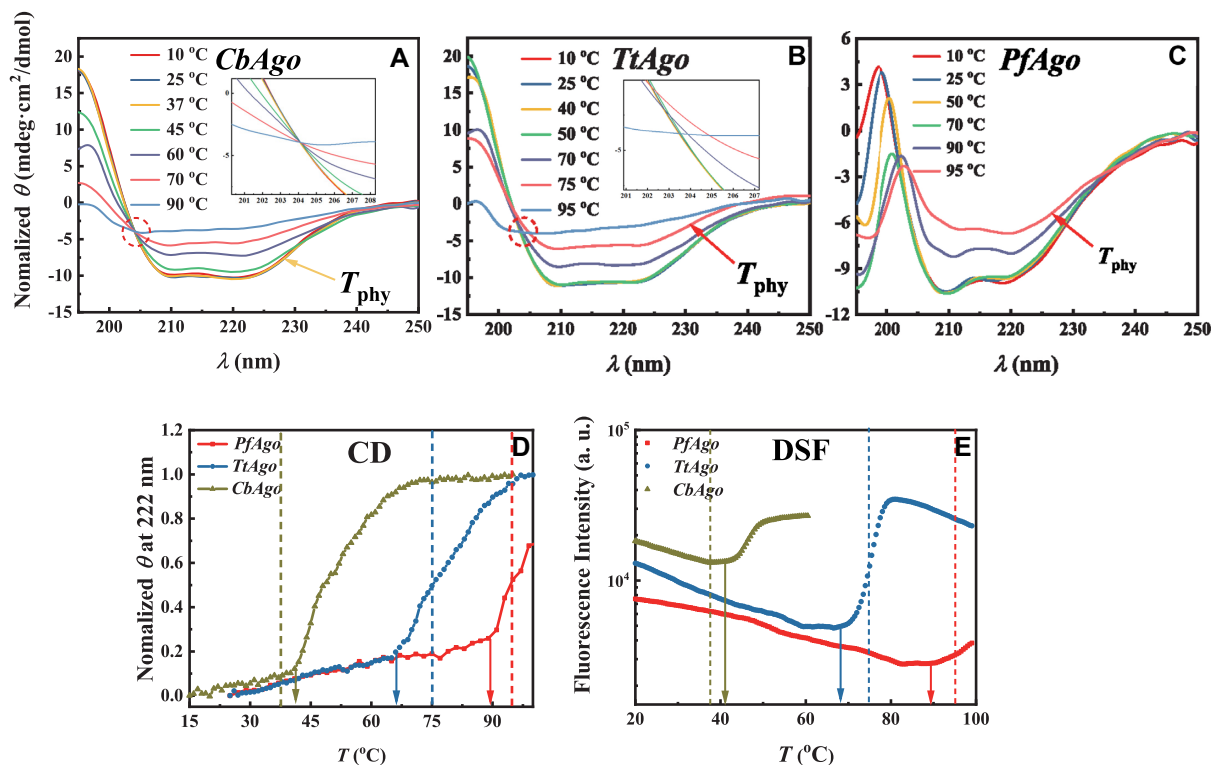


Figure 2. Structural analysis of tertiary and secondary structures in *PfAgo*, *TtAgo* and *CbAgo* at distinct temperatures obtained from far-UV CD spectroscopy and DSF spectroscopy. Far-UV CD spectra of (A) *CbAgo*, (B) *TtAgo* and (C) *PfAgo* measured at different temperatures. The insets in (A) and (B) are enlarged views showing intersecting portions of the far-UV CD spectra. The well-defined isochromatic point is only present in (A), indicating that the two-state scenario only works for the thermal unfolding process of *CbAgo*. Thermal unfolding curves of the three pAgos measured by (D) far-UV CD spectroscopy and by (E) DSF spectroscopy. The solid arrows and dashed lines in (D) and (E) represent T_{on} and T_{phy} , respectively.

values ($qR_g > 3$) (see Figure 3B and C). In other words, the scattering plots at their corresponding T_{phy} are intermediate between that of globular protein (lysozyme) and that of a fully unfolded protein (IDP). This comparison indicates that the two thermophilic pAgos are partially melted at T_{phy} (48–50,52). A plausible scheme is that the internal packing of the thermophilic pAgos is loosening with some of the secondary structure, and none of the domain is completely unfolded to random coils. This result is indeed supported by far-UV CD results in Figure 2 and supported by the *ab initio* low-resolution structure reconstructed from SAXS data (28) (see Figure 3D–F, the detailed comparisons of model and SAXS data at different temperatures are presented in Supplementary Figures S13–S15, *ab initio* model is presented in Supplementary Figure S16). Moreover, such a partially-disrupted structure will inevitably increase the overall size of the protein, which is supported by the results of the radius of gyration, R_g , determined by the slope of the low- q results of SAXS (52). As shown in Figure 3G, R_g of thermophilic pAgos at T_{phy} is significantly larger than those measured at room temperature, whereas *CbAgo* maintains its R_g from room temperature to its T_{phy} (the Guinier plots of proteins at different temperatures are shown in Supplementary Figures S13–S15). We also estimated the molecular weight (M_w) of proteins estimated from SAXS data at different temperatures (47). As shown in Supplementary Table S3, the M_w of proteins at different temperatures is ap-

proximately the same with as the M_w estimated from the amino acid sequence, which indicates that the pAgos remain monomeric at moderate and elevated temperatures.

Furthermore, we compared the structural flexibility of thermophilic pAgos at 25°C with respect to that at T_{phy} by applying Porod-Debye analysis to the SAXS data (45,46), which is the product of the scattering intensity and the fourth power of the scattering wavevector, $q^4 \cdot I(q)$. As shown in Figure 3H and I, the $q^4 \cdot I(q)$ of *PfAgo* and *TtAgo* measured at 25°C show a clear Porod plateau (guided by the gray dashed line, indicating a compact rigid conformation), whereas the profiles measured at T_{phy} grow continuously without forming a plateau, revealing rather flexible structures. The above comparison in Figure 3H and I indicates that the partially-melted structure of both *PfAgo* and *TtAgo* at T_{phy} has much greater flexibility than the well-folded form at 25°C (45,46). In addition, we also compared the structural flexibility of *CbAgo* with respect to *PfAgo* and *TtAgo* at 25°C by the analysis of B-factors derived from crystal structure and MD simulation. As shown in Figure 1 and Supplementary Figure S4 and S5, the B-factors of *CbAgo* are larger than those of the two thermophilic pAgos, revealing that *CbAgo* is more flexible at room temperature than the two thermophilic pAgos. The results might also rationalize why *CbAgo* can achieve high cleavage activity at moderate temperature, as the required flexibility might already be achieved therein.

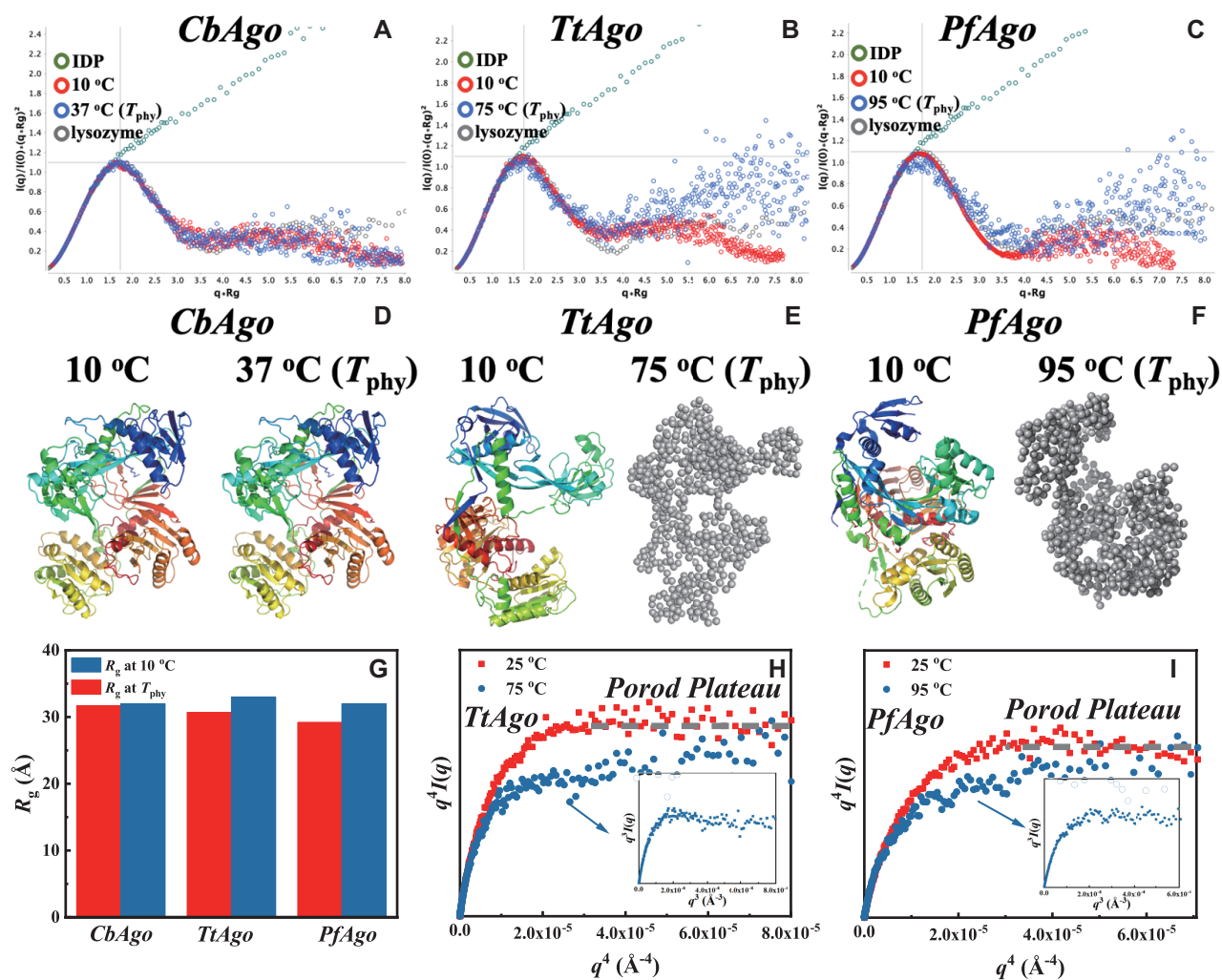


Figure 3. Structures and dynamics of *PfAgo*, *TtAgo* and *CbAgo* at moderate and elevated temperatures obtained from SAXS. Dimensionless Kratky plots of (A) *CbAgo*, (B) *TtAgo* and (C) *PfAgo* at different temperatures. The gray circles and green circles represent the SAXS data of globular protein (lysozyme, SASDBD ID: SASDMG2) and intrinsically disordered protein (SASDBD ID: SASDEE2), respectively for comparison. The atomic model and *ab initio* model of (D) *CbAgo*, (E) *TtAgo* and (F) *PfAgo* at 10 °C and T_{phy} . A comparison between the SAXS profile of proteins and the scattering profile obtained from the model is presented in Supplementary Figures S13–S15. (G) R_g of *PfAgo*, *TtAgo* and *CbAgo* at 10 °C and T_{phy} obtained from SAXS. The Guinier plots of proteins at different temperatures are shown in Supplementary Figure S13–S15. Porod-Debye analysis, $q^4 I(q)$, of (H) *PfAgo* and (I) *TtAgo* at 25 °C and T_{phy} . Transforming proteins at T_{phy} by $q^3 I(q)$ vs. q^3 (inset in Figure 3h and i) verifies that the intensity decay is no longer q^{-4} but q^{-3} . The details about the SAXS data collection and analysis are summarized in Supplementary Table S5.

The enzymatic functional role of the partially-disrupted structure of the thermophilic pAgos. Combining Figures 2 and 3 and Supplementary Figure S14–S16, one can conclude that thermophilic pAgos assume loosely-packed and partially-disrupted dynamical structures at T_{phy} , which are different from the compact crystalline structure determined by X-ray crystallography at moderate temperatures. In contrast, the compact crystalline structure is the functional form of *CbAgo* at its T_{phy} . The intriguing question thus arises as to whether the partially-disrupted structure and the high cleavage activity of thermophilic pAgos is a coincidence at T_{phy} that both result from the elevated temperature. To address this question, we partially unfolded the structure of thermophilic pAgos by incubating them with a certain concentration of denature agent, urea. As shown in Figure 4A–D, the addition of urea significantly disrupts

the structure of the two thermophilic pAgos, lowers T_{on} by $\sim 5^\circ\text{C}$ (Figure 4A and B) and substantially increases their structural flexibility (Figure 4C and D). More importantly, such treatment also greatly promotes the cleavage activity on the target ssDNA for *TtAgo* below 80 °C and for *PfAgo* from 90 to 100 °C (see Figure 4E–F and Supplementary Figures S17 and S18).

Combining Figures 2 to 4, one can deduce that adding urea and increasing the temperature can both partially disrupt the structure of the thermophilic pAgos and subsequently enhance their DNA-cleavage activity. In contrast, we also incubated *CbAgo* with urea to partially unfold it (Supplementary Figure S19), and the obtained cleavage efficiency was significantly suppressed (see in Supplementary Figures S20, S21, S35 and Supplementary Table S4). Hence, the partially disrupted structure only benefits the

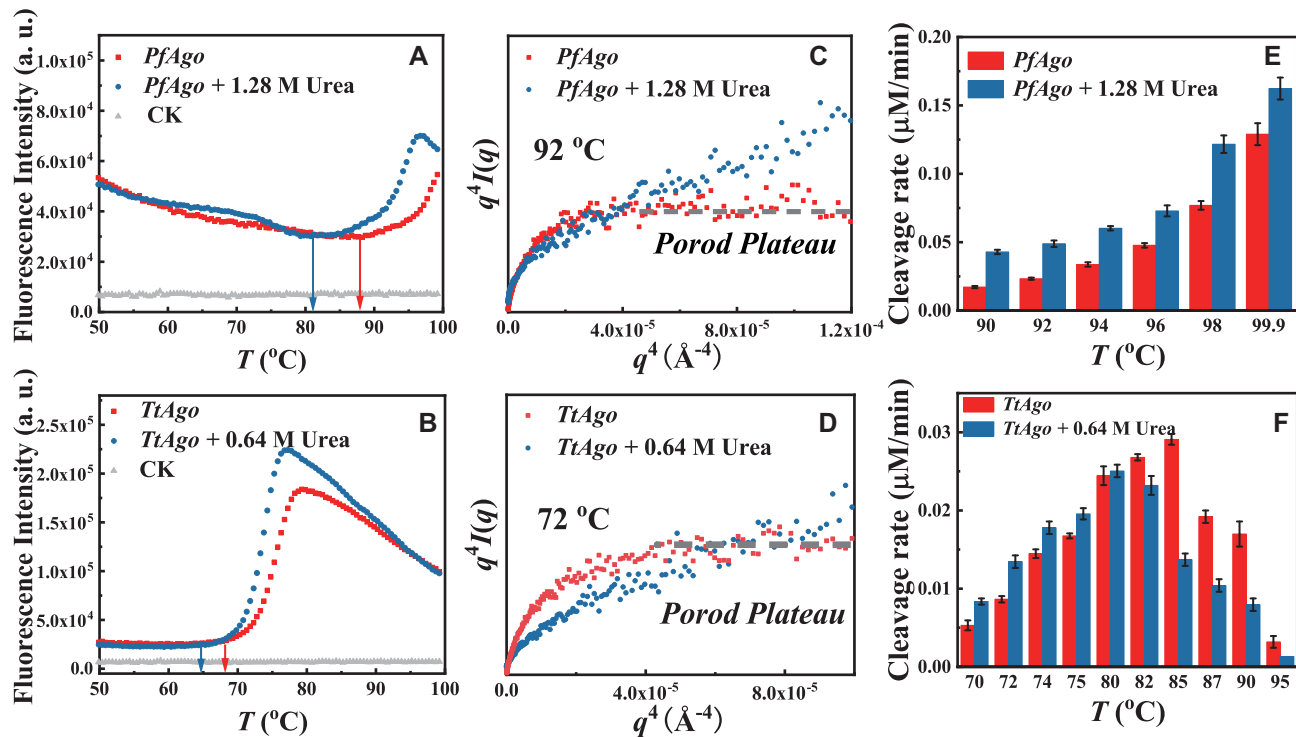


Figure 4. The key role of the partially-disrupted structure of thermophilic pAgos for cleavage of the ssDNA target at elevated temperatures. The thermal unfolding curves of (A) *PfAgo* and (B) *TtAgo* with and without incubation with urea as a function of temperature obtained from DSF. The arrow indicates the value of T_{on} . The CK in (A) and (B) represents the mixture of urea and dye molecules without proteins, revealing that the observed temperature dependence of the fluorescence signals above is not caused by the interaction between the urea and dye molecules. Porod-Debye plots of (C) *PfAgo* and (D) *TtAgo* with and without urea. Cleavage activity of (E) *PfAgo* with and without 1.28 M urea and (F) *TtAgo* with and without 0.64 M urea, which was loaded with ssDNA guide and then incubated with ssDNA target in a 1:10:5 molar ratio (protein:guide:target). These activities are determined as the maximum slope of the time dependence of fluorescence intensity resulting from the cleavage function before it reaches the plateau (see Supplementary Figures S17 and S18) (65). Three samples were used for each experimental condition. The results from three independent experiments were quantified. Error bars represent the standard deviations of three independent experiments. We note that the cleavage activity presented in (E) and (F) was obtained by using this fluorescence method instead of gel diagram analysis, as the former is more accurate (65). The detailed procedure is presented in the Materials and Methods. Supplementary Figure S23 is another control experiment, revealing that urea by itself cannot degrade the target ssDNA. The nucleotide sequences of the guide and target ssDNAs are presented in Supplementary Figures S17 and S18. The cleavage activity of *CbAgo* incubated with 0.64 M urea at 37°C is shown in Supplementary Figures S36 and S37 for comparison, such a low concentration of urea at such low temperature can affect neither the structure nor the activity of *CbAgo*.

functionality of the thermophilic pAgos. To further prove that structural disruption is crucial for the functionality of thermophilic pAgos, we examined the cleavage activity of *PfAgo* and *TtAgo* incubated with similar amounts of urea used as in Figure 4 but at slightly lower temperatures to prevent appreciable structural disruption. As shown in Supplementary Figure S22, the DNA-cleavage activity of the obtained thermophilic pAgos remains intact as compared to that without incubation with urea. Therefore, partially disrupting the structure of thermophilic pAgos is the key for it to reach the high cleavage activity, whereas the best functional state of the mesophilic counterpart, *CbAgo*, is the crystalline form.

For pAgos to conduct the catalytic function, it binds to the target first and then performs the cleavage function. The intriguing question arises as to whether the partially-disrupted structure facilitates the binding of the thermophilic pAgos to the target or promotes the cleavage function. Here, we quantified the biofunction of the protein by using the Michaelis-Menten kinetics model (53). As shown in Table 1, we found that k_{cat} of pAgos is enhanced by a factor of 2.5 by the presence of urea, whereas the effect

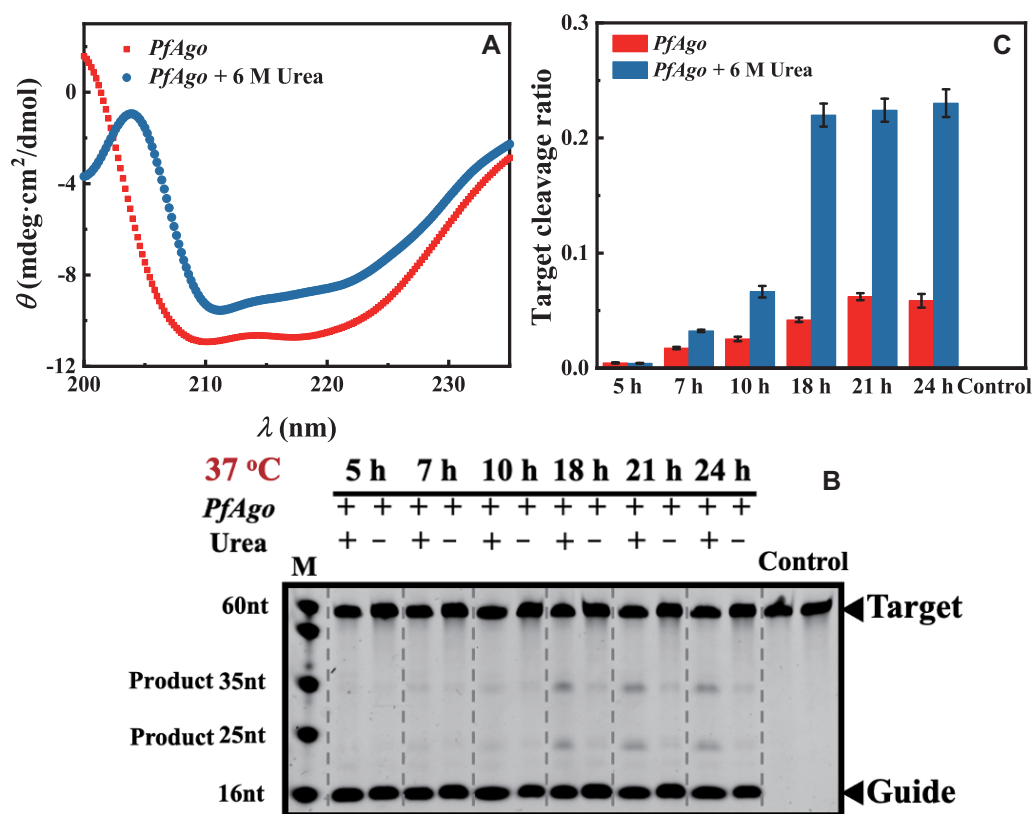
on K_M is rather small and falls in the experimental error. Thus, one can deduce that the partially-disrupted structure of thermophilic pAgos primarily enhances the cleavage efficiency, and does not greatly affect the affinity of the protein to the substrates.

We extended the test to human body temperature, where the *PfAgo* is incubated with 6 M urea for 24 h at 37°C, and the structure of *PfAgo* is partially disrupted (see in Figure 5A). Interestingly, the obtained *PfAgo* enhances the cleavage activity by 5-fold when observed over 24 h at 37°C (see in Figure 5B and C), which is >50°C below the T_{phy} value of the protein. This result is striking and firmly proves that the partially-disrupted structure plays a key role in facilitating the catalytic activity of thermophilic pAgos.

Partially-disrupted state in thermophilic pAgo derived from MD simulations. To further understand how urea disrupted the structure of thermophilic pAgos, we carried out all-atom MD simulations on *PfAgo* with and without 6 M urea at 37°C to mimic the experimental conditions. The SAXS scattering profile calculated from MD simulation agrees quantitatively with the experimental profile (see Sup-

Table 1. Michaelis–Menten analysis of *PfAgo* and *TtAgo* with and without the presence of urea. The results of k_{cat} and K_M are obtained from Supplementary Figure S24. Means and standard deviations (error bars) were obtained from three independent measurements

Protein	T ($^{\circ}\text{C}$)	K_M (μM)	k_{cat} (min^{-1})	k_{cat}/K_M ($\mu\text{M}^{-1}\cdot\text{min}^{-1}$)
<i>PfAgo</i>	95	0.82 ± 0.24	0.60 ± 0.058	0.73
<i>PfAgo</i> + 1.28 M Urea	95	1.2 ± 0.27	1.5 ± 0.16	1.3
<i>TtAgo</i>	70	1.5 ± 0.28	0.058 ± 0.0031	0.039
<i>TtAgo</i> + 0.64 M Urea	70	1.4 ± 0.33	0.14 ± 0.012	0.10

**Figure 5.** Experimental results of *PfAgo* with and without incubation with urea at 37°C. (A) Far-UV CD spectra of *PfAgo* with and without 6 M urea. (B) *PfAgo* shows much greater cleavage activity after 10 h. Here, *PfAgo* is loaded with a 16 nt ssDNA as a guide and a 60 nt ssDNA as a target in a 1:10:5 molar ratio (*PfAgo* : guide : target). Products were resolved on 16% denaturing polyacrylamide gels. (C) Quantifying the effects of incubating with urea on cleavage activity by gel SDS-PAGE analysis. Three samples were used for each experimental condition. The results from three independent experiments were quantified. Error bars represent the standard deviations of three independent experiments. Cleavage activity determined by SDS-PAGE analysis is not as accurate as in Supplementary Figures S17 and S18 by monitoring fluorescence. However, the fluorescence method cannot be used in this case as the experimental time scale (5–24 h) is too long.

plementary Figure S25), demonstrating that the partially-disrupted *PfAgo* obtained experimentally after incubation with 6 M urea can be described by the MD-derived structures (a snapshot of the MD simulation box is presented in Supplementary Figure S26, and the potential energy as a function of the MD trajectory time of protein is presented in Supplementary Figure S27). In Figure 6A, we compared the most representative structure of *PfAgo* with (blue) and without (red) urea derived from MD and found that the addition of urea significantly reduced the number of hydrogen bonds and salt bridges both globally (Figure 6B) and locally around the catalytic site (Figure 6C and Supplementary Figure S28). Interestingly, after adding urea, the number of remaining salt bridges and hydrogen bonds in *PfAgo* approximates that of pristine *CbAgo* (Figure 6B and C), which

will significantly promote the flexibility of *PfAgo* at 37°C. A closer examination revealed that the salt bridges and hydrogen bonds were mostly broken on the protein surface due to the presence of urea (Supplementary Figure S31a), whereas these inter-residue interactions inside the protein core remained intact (Supplementary Figure S31b). Breaking these important inter-residue interactions on the protein surface not only loosens the packing of residues, i.e. an increased R_g (comparing Figure 6d and e), but also locally disrupts some of the secondary structures. For instance, the alpha-helix in N domain (blue circle region in Figure 6A) and the one in linker 2 (green circle region in Figure 6A) are melted, and the loop in the MID domain is more extended and relaxing (gray circle region in Figure 6A). Overall, the flexibility of the N domain, PAZ domain, MID do-

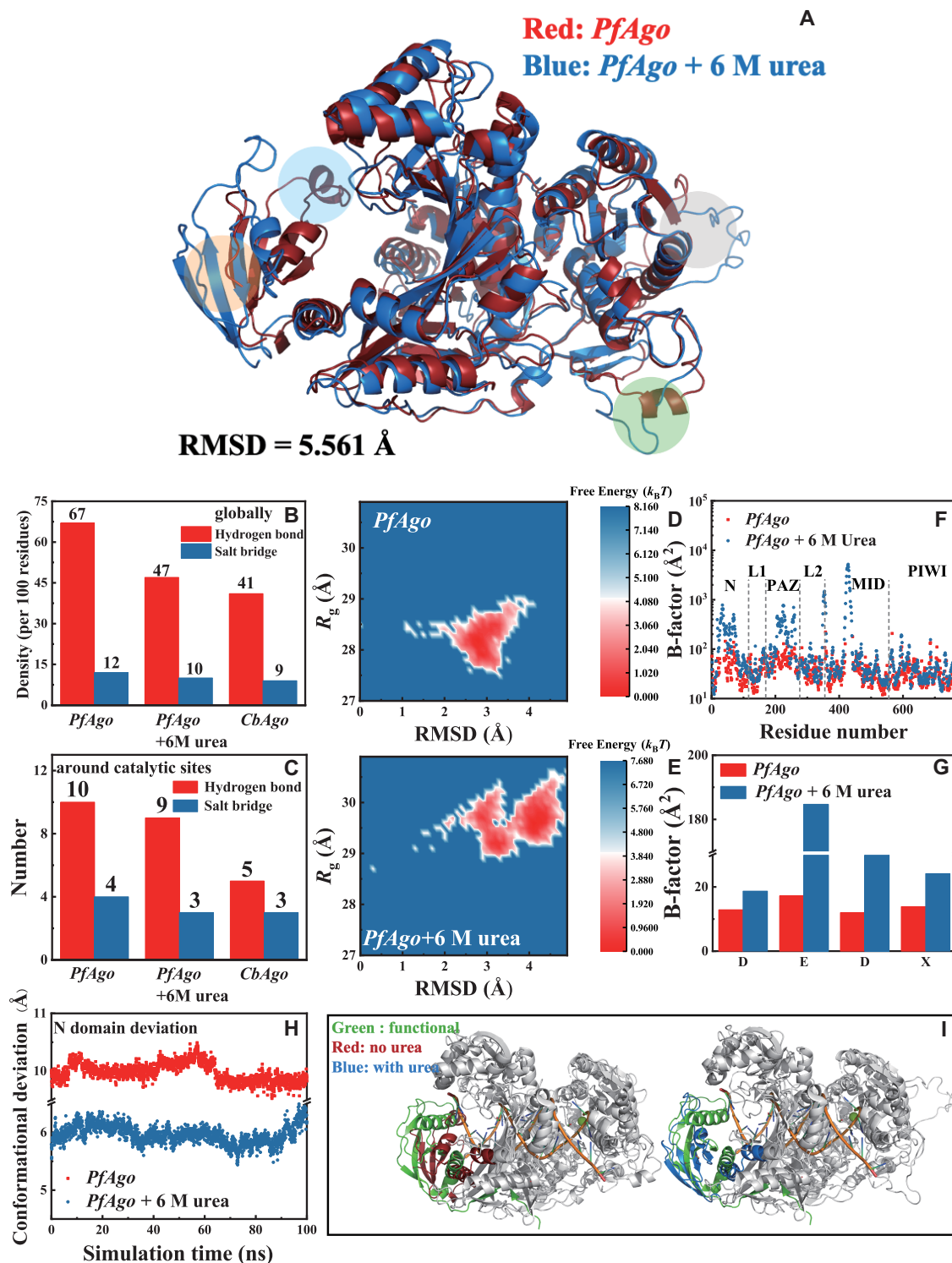


Figure 6. MD simulation results of *PfAgo* with and without 6 M urea at 37°C. (A) Superposition of the MD-derived structure of *PfAgo* with (blue) and without (red) the presence of urea. The simulation system does not include ssDNA guide, ssDNA target or Mn^{2+} . The semitransparent circles highlight the regions where the significant changes in local structure occur when urea is added. The alignment on C_{α} is achieved by using PyMOL software. The density of hydrogen bonds and salt bridges (B) globally and (C) around the catalytic sites in *PfAgo* with and without urea. Phase space sampled by MD on *PfAgo* (D) without and (E) with 6 M urea. RMSD is the root mean squared deviation of the structure in the first MD snapshot after equilibration. Comparison of B-factors of (F) the overall structure and (G) catalytic residues with and without urea. (H) Conformational deviations of the N domain in *PfAgo* (with or without urea) from that of the experimental functional form (i.e. the *CbAgo*-guide-target complex with Mg^{2+}), defined as the root mean squared deviations of C_{α} . Here, the overall protein structure is aligned by PyMOL. (I) Structural alignment of *PfAgo* without (left panel) and with (right panel) urea with respect to that of the experimental functional conformation (PDB ID: 6qzk). The N domain in *PfAgo* without urea, with urea, and in the experimental functional form is highlighted in red, blue, and green, respectively.

main, linker 2 and catalytic sites of the thermophilic pAgos are greatly enhanced when urea is present (see Figure 6F and G). The enhanced flexibility is further evident in Figure 6D and E, where we compared the conformational phase space of *PfAgo* sampled in MD with and without urea and found that the presence of urea can allow *PfAgo* to explore a much larger conformational space. Greater flexibility is normally assumed to be important to enhance functionality (54–56). In the present case, for example, the enhanced flexibility, particularly in the linker 2 and the catalytic region, may facilitate the propagation of the duplex between the guide and target DNA strands (23), the conformational restoration of the PAZ and MID domains after target release (22) and the alignment of catalytic sites necessary for cleavage (19).

Moreover, from MD we also found that the urea-induced structural change shifts the protein conformation toward its functional form. As seen in Figure 6H and I, after adding of urea, the position and orientation of the N domain in *PfAgo* are adjusted closer to its functional conformation. Here, the functional conformation of the N domain references that in the X-ray crystalline structure of the *CbAgo*-guide-target complex in the presence of Mg^{2+} (25), where the N domain is ready to unwind the duplex of the guide and target after cleavage (57,58). The above finding suggests that surface-disrupted structures might lower the energy cost for such an important functional step. Similar analysis by referencing the position and orientation of the N domain in the X-ray structure of the *TiAgo*-guide-target complex as the functional form is conducted in Supplementary Figure S32, and one can qualitatively derive the same conclusion that incubating with urea will adjust the N domain closer to its functional state (19).

The above analysis of the MD-derived structure of *PfAgo* with and without urea indicates that the partially-disrupted thermophilic pAgos discovered in the present work correspond to a structure in which the internal core of the protein maintains the structure as in the crystalline one (27) (see Supplementary Figure S31), but the greatest change occurs on the protein surface with many salt bridges and hydrogen bonds being broken and some surface secondary structure getting melted. These changes on the protein surface will loosen the overall packing of the thermophilic pAgos and enhance their flexibility.

As reported in the literature, conformational flexibility is essential for the cleavage function of pAgos such as the rearrangement of catalytic sites, propagation of duplexes, release of the product from the MID and N domains, and changing of the binding site of the 3'-end of the guide from the N to the PAZ domain (19,20,23,38,39). The crystal structure of mesophilic *CbAgo* has many fewer hydrogen bonds and salt bridges than those of thermophilic pAgos. Thus, the function-required internal flexibility at moderate temperatures might already be satisfied in its well-folded crystal form. In contrast, the excess hydrogen bonds and salt bridges in the crystal structure of thermophilic pAgos as well as the resulting secondary structures will certainly restrict the structural flexibility, which might be the key to limiting the activity of thermophilic pAgos at moderate temperatures. We note that these excess inter-residue interac-

tions and resulting secondary structures help stabilize the structure of thermophilic pAgos and ensure that they survive the high-temperature environment. However, to reach high activity under physiological conditions, some of these interactions and structures need to be broken at elevated temperatures (or when incubated with urea) to release sufficient flexibility for function. The present findings reveal an ingenious structural design in which enough hydrogen bonds and salt bridges are present on the protein surface at moderate temperatures to limit the functionality and stabilize the structure of the biomacromolecule, but they are partially melted at elevated temperatures to enhance the flexibility necessary for biological function. In the meantime, the structure of the catalytic core of the protein molecule remains approximately intact throughout the wide temperature range.

Moreover, these surface-disrupted dynamical states of thermophilic pAgos are unlikely to be a specific structure but rather an ensemble of structures. This can provide numerous evolutionary templates for adapting to distinct environments (59–61). Given that the two thermophilic pAgos (*PfAgo* and *TiAgo*) are much closer to the root of the phylogenetic tree than their mesophilic protein (24), it is tempting to speculate that such dynamical states in protein might be superior to highly evolved enzymes with well-defined folded structures as starting points for the directed evolution of tailored catalysts.

In the past, entropy contributions to the thermostability of thermophilic proteins have been studied by several works using neutron scattering to compare the flexibility between thermophilic proteins and their mesophilic counterparts (55,62,63) and even the average flexibility of biomolecules among cells living in different thermal environments from regular to extremely high-temperature conditions (64). A general finding made in these neutron scattering works is that the flexibility is important for the stability of thermophilic biomolecules. Most of these studies demonstrated that thermophilic proteins have greater structural flexibility than their mesophilic counterparts at identical temperatures (55,62,63) and revealed that this flexibility could increase the unfolding free energy barrier to directly stabilize thermophilic proteins (55). We note that the connection between flexibility, stability, and functionality in thermophilic pAgos observed in the present work is different from the findings in these previous works. The previous studies all compared the flexibility between thermophilic and mesophilic proteins at one identical temperature, mostly under ambient conditions (55,62,63). In contrast, the present work demonstrates that under the same ambient conditions, thermophilic pAgos are stiffer than their mesophilic counterparts, and the high structural flexibility and the associated high activity of the thermophilic pAgos are actually achieved at physiological temperatures, which are much higher than those under ambient conditions. Second, the previous work often compares one thermophilic protein to a mesophilic protein (55,62,63). Instead, the present work found that the partially-melted structure is a general feature for all 6 thermophilic pAgos as we can find. Hence, the partially-melted structure alongside the resulting structural flexibility could be a general sce-

nario adopted by the thermophilic species of this protein family to achieve their high activity.

CONCLUSION

In the present work, we investigated the temperature dependence of structure, dynamics, and endonuclease activity of thermophilic pAgos (*PfAgo* and *TtAgo*) and their mesophilic counterpart *CbAgo* using various experimental and simulation techniques. We made the following discoveries:

1. The two studied thermophilic pAgos (*PfAgo* and *TtAgo*) possess stronger intramolecular interactions, including hydrogen bonds, salt bridges and hydrophobic interactions inside the protein core, globally over the entire protein and locally at the catalytic residues, than the mesophilic *CbAgo*. This renders thermal stability to thermophilic pAgos and strongly reduces their structural flexibility.
2. At physiological temperatures, *PfAgo* and *TtAgo* adopt a loosely-packed dynamical structure with a partially-melted surface which is an intermediate state between the crystalline structure and fully unfolded state, whereas *CbAgo* takes a compact crystalline structure at its optimal function temperature.
3. The partially-disrupted structure breaks many hydrogen bonds, salt bridges, and even some secondary structures on the surface of thermophilic pAgos to release the structural flexibility, leading to high cleavage activity under physiological conditions. This result is supported by the biochemical assays where we disrupted the structure of the two thermophilic pAgos by incubating them with urea and found significantly higher DNA cleavage activity compared to that of the pristine ones. Complementary kinetic analysis revealed that the partially-disrupted structure in thermophilic pAgos promotes its efficiency in cleaving the DNA without affecting its affinity for substrates.

Our findings of thermophilic pAgos assuming loosely-packed dynamical structures with partially-melted surfaces under physiological conditions modify the existing structure-function relationship established based on the compact crystalline structures determined at moderate temperatures. It is not only crucial for understanding the microscopic mechanism of pAgos, but also suggests a smart design for the high-activity thermophilic proteins where a great amount of strong inter-residue interactions is required on the biomolecular surface at moderate temperatures to limit the function and preserve the structural integrity, but part of them is broken at the elevated desired temperatures to release sufficient structural flexibility to reach high activity.

DATA AVAILABILITY

The SASBDB IDs of *PfAgo*, *TtAgo* and *CbAgo* are presented in Supplementary Table S5 in SI. All other data are presented in SI.

SUPPLEMENTARY DATA

Supplementary Data are available at NAR Online.

ACKNOWLEDGEMENTS

We would like to thank Dr Yongjia Liu and Dr Ruibin Wang from Instrumental Analysis Center of Shanghai Jiao Tong University for assistance with thermal performance tests via nanoDSC and CD spectroscopy. We would like to thank Dr Na Li from BL19U2 beamline of Shanghai Synchrotron Radiation Facility (SSRF) for the help with synchrotron X-ray measurements on No. h20pr0008. We would also like to thank Prof. Yuhang Zhang for inspiring discussions. We acknowledge the support by the Student Innovation Center and the High Performance Computing Center at Shanghai Jiao Tong University. L. Zheng thanks Master degree candidate Nuolan Li for conducting the biochemical experiments.

Author contributions: L.H., Q.L. and Y.F. supervised the project. L.Z., B.Z., H.Lu. and J.H. prepared the samples. B.Z. and L.Z. designed and performed nanoDSC, DSF measurement and circular dichroism spectroscopy. H.Lu., B.Z., and L.Z. performed the biochemical experiments. L.Z. and B.Z. performed the SAXS experiments. B.Z., S.L., H.Liu. and L.Z. performed MD simulations.

FUNDING

NSF China [11504231, 31630002, 22063007]; Innovation Program of Shanghai Municipal Education Commission, National Key Research & Development Program of China [2018YFA0900403]; Shanghai Pilot Program for Basic Research-Shanghai Jiao Tong University [21TQ1400204]. Funding for open access charge: NSF China.

Conflict of interest statement. None declared.

REFERENCES

1. Wu, L. and Qu, X. (2015) Cancer biomarker detection: recent achievements and challenges. *Chem. Soc. Rev.*, **44**, 2963–2997.
2. Choi, J.R., Hu, J., Tang, R., Gong, Y., Feng, S., Ren, H., Wen, T., Li, X., Wan Abas, W.A.B., Pingguan-Murphy, B. *et al.* (2016) An integrated paper-based sample-to-answer biosensor for nucleic acid testing at the point of care. *Lab Chip*, **16**, 611–621.
3. Mumford, R.A., Macarthur, R. and Boonham, N. (2016) The role and challenges of new diagnostic technology in plant biosecurity. *Food Secur.*, **8**, 103–109.
4. Gootenberg, J.S., Abudayyeh, O.O., Lee, J.W., Essletzbichler, P., Dy, A.J., Joung, J., Verdine, V., Donghia, N., Daringer, N.M., Freije, C.A. *et al.* (2017) Nucleic acid detection with CRISPR-Cas13a/C2c2. *Science*, **356**, 438–442.
5. Komor, A.C., Badran, A.H. and Liu, D.R. (2017) CRISPR-based technologies for the manipulation of eukaryotic genomes. *Cell*, **168**, 20–36.
6. Barrangou, R. and Doudna, J.A. (2016) Applications of CRISPR technologies in research and beyond. *Nat. Biotechnol.*, **34**, 933–941.
7. Wu, W.Y., Lebbink, J.H., Kanaar, R., Geijsen, N. and Van Der Oost, J. (2018) Genome editing by natural and engineered CRISPR-associated nucleases. *Nat. Chem. Biol.*, **14**, 642–651.
8. Li, Y., Li, S., Wang, J. and Liu, G. (2019) CRISPR/Cas systems towards next-generation biosensing. *Trends Biotechnol.*, **37**, 730–743.
9. Hegge, J.W., Swarts, D.C. and van der Oost, J. (2018) Prokaryotic argonaute proteins: novel genome-editing tools? *Nat. Rev. Microbiol.*, **16**, 5–11.
10. Song, J., Hegge, J.W., Mauk, M.G., Chen, J., Till, J.E., Bhagwat, N., Azink, L.T., Peng, J., Sen, M., Mays, J. *et al.* (2020) Highly specific

- enrichment of rare nucleic acid fractions using thermus thermophilus argonaute with applications in cancer diagnostics. *Nucleic Acids Res.*, **48**, e19.
11. He, R., Wang, L., Wang, F., Li, W., Liu, Y., Li, A., Wang, Y., Mao, W., Zhai, C. and Ma, L. (2019) Pyrococcus furiosus Argonaute-mediated nucleic acid detection. *Chem. Commun.*, **55**, 13219–13222.
 12. Liu, Q., Guo, X., Xun, G., Li, Z., Chong, Y., Yang, L., Wang, H., Zhang, F., Luo, S., Cui, L. et al. (2021) Argonaute integrated single-tube PCR system enables supersensitive detection of rare mutations. *Nucleic Acids Res.*, **49**, e75.
 13. Wang, J., Li, J., Zhao, H., Sheng, G., Wang, M., Yin, M. and Wang, Y. (2015) Structural and mechanistic basis of PAM-dependent spacer acquisition in CRISPR-Cas systems. *Cell*, **163**, 840–853.
 14. Hegge, J.W., Swarts, D.C. and van der Oost, J. (2018) Prokaryotic argonaute proteins: novel genome-editing tools? *Nat. Rev. Microbiol.*, **16**, 5–11.
 15. Enghiad, B. and Zhao, H. (2017) Programmable DNA-guided artificial restriction enzymes. *ACS Synth. Biol.*, **6**, 752–757.
 16. Swarts, D.C., Makarova, K., Wang, Y., Nakanishi, K., Ketting, R.F., Koonin, E.V., Patel, D.J. and van der Oost, J. (2014) The evolutionary journey of argonaute proteins. *Nat. Struct. Mol. Biol.*, **21**, 743–753.
 17. Swarts, D.C., Jore, M.M., Westra, E.R., Zhu, Y., Janssen, J.H., Sniijders, A.P., Wang, Y., Patel, D.J., Berenguer, J. and Brouns, S.J. (2014) DNA-guided DNA interference by a prokaryotic argonaute. *Nature*, **507**, 258–261.
 18. Yuan, Y.-R., Pei, Y., Ma, J.-B., Kuryavyi, V., Zhadina, M., Meister, G., Chen, H.-Y., Dauter, Z., Tuschl, T. and Patel, D.J. (2005) Crystal structure of a. aeolicus argonaute, a site-specific DNA-guided endoribonuclease, provides insights into RISC-Mediated mRNA cleavage. *Mol. Cell*, **19**, 405–419.
 19. Sheng, G., Zhao, H., Wang, J., Rao, Y., Tian, W., Swarts, D.C., van der Oost, J., Patel, D.J. and Wang, Y. (2014) Structure-based cleavage mechanism of thermus thermophilus argonaute DNA guide strand-mediated DNA target cleavage. *Proc. Natl. Acad. Sci. U.S.A.*, **111**, 652–657.
 20. Willkomm, S., Oellig, C.A., Zander, A., Restle, T., Keegan, R., Grohmann, D. and Schneider, S. (2017) Structural and mechanistic insights into an archaeal DNA-guided argonaute protein. *Nat. Microbiol.*, **2**, 17035.
 21. Miyoshi, T., Ito, K., Murakami, R. and Uchiumi, T. (2016) Structural basis for the recognition of guide RNA and target DNA heteroduplex by argonaute. *Nat. Commun.*, **7**, 11846.
 22. Lisitskaya, L., Aravin, A.A. and Kulbachinskiy, A. (2018) DNA interference and beyond: structure and functions of prokaryotic argonaute proteins. *Nat. Commun.*, **9**, 5165.
 23. Wang, Y., Juranek, S., Li, H., Sheng, G., Wardle, G.S., Tuschl, T. and Patel, D.J. (2009) Nucleation, propagation and cleavage of target RNAs in ago silencing complexes. *Nature*, **461**, 754–761.
 24. Swarts, D.C., Hegge, J.W., Hinojo, I., Shiimori, M., Ellis, M.A., Dumrongkulraksa, J., Terns, R.M., Terns, M.P. and van der Oost, J. (2015) Argonaute of the archaeon pyrococcus furiosus is a DNA-guided nuclease that targets cognate DNA. *Nucleic Acids Res.*, **43**, 5120–5129.
 25. Hegge, J.W., Swarts, D.C., Chandradoss, S.D., Cui, Tao, J., Kneppers, J., Jinek, M., Joo, C. and van der Oost, J. (2019) DNA-guided DNA cleavage at moderate temperatures by clostridium butyricum argonaute. *Nucleic Acids Res.*, **47**, 5809–5821.
 26. Liu, Y., Li, W., Jiang, X., Wang, Y., Zhang, Z., Liu, Q., He, R., Chen, Q., Yang, J., Wang, L. et al. (2021) A programmable omnipotent argonaute nuclease from mesophilic bacteria kurthia massiliensis. *Nucleic Acids Res.*, **49**, 1597–1608.
 27. Rivas, F.V., Tolia, N.H., Song, J.J., Aragon, J.P., Liu, J., Hannon, G.J. and Joshua-Tor, L. (2005) Purified argonaute2 and an siRNA form recombinant human RISC. *Nat. Struct. Mol. Biol.*, **12**, 340–349.
 28. Svergun, D.I., Petoukhov, M.V. and Koch, M.H.J. (2001) Determination of domain structure of proteins from X-Ray solution scattering. *Biophys. J.*, **80**, 2946–2953.
 29. Svergun, D., Barberato, C. and Koch, M.H.J. (1995) CRY SOL - a Program to evaluate X-ray solution scattering of biological macromolecules from atomic coordinates. *J. Appl. Crystallogr.*, **28**, 768–773.
 30. Huang, J., Rauscher, S., Nawrocki, G., Ran, T., Feig, M., de Groot, B.L., Grubmüller, H. and MacKerell, A.D. (2017) CHARMM36m: an improved force field for folded and intrinsically disordered proteins. *Nat. Methods*, **14**, 71–73.
 31. Hess, B., Kutzner, C., van der Spoel, D. and Lindahl, E. (2008) GROMACS 4: algorithms for highly efficient, load-balanced, and scalable molecular simulation. *J. Chem. Theory Comput.*, **4**, 435–447.
 32. Essmann, U., Perera, L., Berkowitz, M.L., Darden, T., Lee, H. and Pedersen, L.G. (1995) A smooth particle mesh ewald method. *J. Chem. Phys.*, **103**, 8577–8593.
 33. Bussi, G., Donadio, D. and Parrinello, M. (2007) Canonical sampling through velocity rescaling. *J. Chem. Phys.*, **126**, 014101.
 34. Parrinello, M. and Rahman, A. (1981) Polymorphic transitions in single crystals: a new molecular dynamics method. *J. Appl. Phys.*, **52**, 7182–7190.
 35. Vanommeslaeghe, K. and MacKerell, A.D. (2012) Automation of the CHARMM general force field (CGenFF) I: bond perception and atom typing. *J. Chem. Inform. Model.*, **52**, 3144–3154.
 36. Vanommeslaeghe, K., Raman, E.P. and MacKerell, A.D. (2012) Automation of the CHARMM general force field (CGenFF) II: assignment of bonded parameters and partial atomic charges. *J. Chem. Inform. Model.*, **52**, 3155–3168.
 37. Song, J.-J., Smith, S.K., Hannon, G.J. and Joshua-Tor, L. (2004) Crystal structure of argonaute and its implications for RISC slicer activity. *Science*, **305**, 1434.
 38. Wang, Y., Sheng, G., Juranek, S., Tuschl, T. and Patel, D.J. (2008) Structure of the guide-strand-containing argonaute silencing complex. *Nature*, **456**, 209–213.
 39. Swarts, D.C., Szczepaniak, M., Sheng, G., Chandradoss, S.D., Zhu, Y., Timmers, E.M., Zhang, Y., Zhao, H., Lou, J., Wang, Y. et al. (2017) Autonomous generation and loading of DNA guides by bacterial argonaute. *Mol. Cell*, **65**, 985–998.
 40. Dominy, B.N., Minoux, H. and Brooks III, C.L. (2004) An electrostatic basis for the stability of thermophilic proteins. *Proteins Struct. Funct. Bioinf.*, **57**, 128–141.
 41. Sterpone, F. and Melchionna, S. (2012) Thermophilic proteins: insight and perspective from in silico experiments. *Chem. Soc. Rev.*, **41**, 1665–1676.
 42. Gursky, O. and Atkinson, D. (1996) Thermal unfolding of human high-density apolipoprotein A-1: implications for a lipid-free molten globular state. *Proc. Natl. Acad. Sci. U.S.A.*, **93**, 2991.
 43. Kuwajima, K. (1989) The molten globule state as a clue for understanding the folding and cooperativity of globular-protein structure. *Proteins Struct. Funct. Bioinf.*, **6**, 87–103.
 44. Ptitsyn, O.B. (1995) In: Anfinsen, C.B., Richards, F.M., Edsall, J.T. and Eisenberg, D.S. (eds). *Advances in Protein Chemistry*. Academic Press, Vol. **47**, pp. 83–229.
 45. Rambo, R.P. and Tainer, J.A. (2011) Characterizing flexible and intrinsically unstructured biological macromolecules by SAS using the porod-debye law. *Biopolymers*, **95**, 559–571.
 46. Rambo, R.P. and Tainer, J.A. (2013) Super-resolution in solution X-ray scattering and its applications to structural systems biology. *Annu. Rev. Biophys.*, **42**, 415–441.
 47. Rambo, R.P. and Tainer, J.A. (2013) Accurate assessment of mass, models and resolution by small-angle scattering. *Nature*, **496**, 477–481.
 48. Kikhney, A.G. and Svergun, D.I. (2015) A practical guide to small angle X-ray scattering (SAXS) of flexible and intrinsically disordered proteins. *FEBS Lett.*, **589**, 2570–2577.
 49. Schroer, M.A., Paulus, M., Jeworrek, C., Krywka, C., Schmacke, S., Zhai, Y., Wieland, D.C., Sahle, C.J., Chimenti, M., Royer, C.A. et al. (2010) High-pressure SAXS study of folded and unfolded ensembles of proteins. *Biophys. J.*, **99**, 3430–3437.
 50. Bernado, P. and Svergun, D.I. (2012) Structural analysis of intrinsically disordered proteins by small-angle X-ray scattering. *Mol. Biosyst.*, **8**, 151–167.
 51. Saw, W.G., Tria, G., Gruber, A., Subramanian Manimekalai, M.S., Zhao, Y., Chandramohan, A., Srinivasan Anand, G., Matsui, T., Weiss, T.M., Vasudevan, S.G. et al. (2015) Structural insight and flexible features of NS5 proteins from all four serotypes of dengue virus in solution. *Acta Crystallogr. Section D*, **71**, 2309–2327.
 52. Feigin, L. and Svergun, D.I. (1987) In: *Structure Analysis by Small-Angle X-ray and Neutron Scattering*. Springer.
 53. Johnson, K.A. and Goody, R.S. (2011) The original michaelis constant: translation of the 1913 Michaelis–Menten paper. *Biochemistry*, **50**, 8264–8269.

54. Henzler-Wildman, K. and Kern, D. (2007) Dynamic personalities of proteins. *Nature*, **450**, 964–972.
55. Liu, Z., Lemmonds, S., Huang, J., Tyagi, M., Hong, L. and Jain, N. (2018) Entropic contribution to enhanced thermal stability in the thermostable P450 CYP119. *Proc. Natl. Acad. Sci. USA*, **115**, E10049.
56. Berendsen, H.J.C. and Hayward, S. (2000) Collective protein dynamics in relation to function. *Curr. Opin. Struct. Biol.*, **10**, 165–169.
57. Kwak, P.B. and Tomari, Y. (2012) The n domain of argonaute drives duplex unwinding during RISC assembly. *Nat. Struct. Mol. Biol.*, **19**, 145–151.
58. Miyoshi, T., Ito, K., Murakami, R. and Uchiumi, T. (2016) Structural basis for the recognition of guide RNA and target DNA heteroduplex by argonaute. *Nat. Commun.*, **7**, 11846.
59. James, L.C. and Tawfik, D.S. (2003) Conformational diversity and protein evolution – a 60-year-old hypothesis revisited. *Trends Biochem. Sci.*, **28**, 361–368.
60. Honaker, M.T., Acchione, M., Zhang, W., Mannervik, B. and Atkins, W.M. (2013) Enzymatic detoxication, conformational selection, and the role of molten globule active sites*. *J. Biol. Chem.*, **288**, 18599–18611.
61. DeGrado, W.F. (1993) Catalytic molten globules. *Nature*, **365**, 488–489.
62. Fitter, J. and Heberle, J. (2000) Structural equilibrium fluctuations in mesophilic and thermophilic α -Amylase. *Biophys. J.*, **79**, 1629–1636.
63. Meinhold, L., Clement, D., Tehei, M., Daniel, R., Finney, J.L. and Smith, J.C. (2008) Protein dynamics and stability: the distribution of atomic fluctuations in thermophilic and mesophilic dihydrofolate reductase derived using elastic incoherent neutron scattering. *Biophys. J.*, **94**, 4812–4818.
64. Tehei, M., Franzetti, B., Madern, D., Ginzburg, M., Ginzburg, B.Z., Giudici-Orticoni, M.-T., Bruschi, M. and Zaccai, G. (2004) Adaptation to extreme environments: macromolecular dynamics in bacteria compared in vivo by neutron scattering. *EMBO Rep.*, **5**, 66–70.
65. Xun, G., Liu, Q., Chong, Y., Guo, X., Li, Z., Li, Y., Fei, H., Li, K. and Feng, Y. (2021) Argonaute with stepwise endonuclease activity promotes specific and multiplex nucleic acid detection. *Bioresour. Bioprocess.*, **8**, 46.